JOURNAL OF ENVIRONMENTAL SCIENCES 95 (2020) 82–90

Available online at www.sciencedirect.com

ScienceDirect

www.elsevier.com/locate/jes

JES JOURNAL OF ENVIRONMENTAL SCIENCES

www.jesc.ac.cn

Exploring the formation potential and optical properties of secondary organic aerosol from the photooxidation of selected short aliphatic ethers

*Jianqiang Zhu, Jianlong Li, Lin Du**

Environment Research Institute, Shandong University, Qingdao 266237, China

ARTICLE INFO

Article history:
Received 30 September 2019
Revised 20 March 2020
Accepted 20 March 2020
Available online 16 April 2020

Keywords:
Smog chamber
Aliphatic ethers
Secondary organic aerosol
Ammonium sulfate
Optical properties

ABSTRACT

Secondary organic aerosol (SOA) formation potential for six kinds of short aliphatic ethers has been studied. The size distribution, mass concentration, and yield of SOA formed by ethers photooxidation were determined under different conditions. The results showed that all six ethers can generate SOA via reaction with OH radicals even under no seed and NO_x-free condition. The mass concentration for six seedless experiments was less than 10 μg/m^3 and the SOA yields were all below 1%. The strong increase in the SOA formation was observed when the system contained ammonium sulfate seed particles, while SOA yield decreased under the high-NO_x condition. SOA composition was analyzed using offline methods. Infrared spectra indicated that there are complex components in the particle-phase including carbonyls acid and aldehydes species. Moreover, the aqueous filter extracts were analyzed using ultraviolet-visible spectrometer and fluorescence spectrophotometer. For the fresh methyl *n*-butyl ether SOA, the largest absorption peak occurs at 280 nm and there exists slightly absorption in the 300–400 nm. Excitation-emission matrices display the distinct peak at excitation/emission = 470 nm/480 nm according to the fluorescence spectrum. These findings are important considerations of formation for ether SOA that can eventually be included in atmospheric models.

Introduction

Atmospheric particulate matter (PM) plays significant roles in atmospheric chemistry, global radiation budget, and Earth's climate (Hallquist et al., 2009; Zhang et al., 2015). They can originate from a wide variety of natural and anthropogenic sources. Primary particles are directly emitted in the form of liquids or solids from biomass burning, incomplete combustion of fossil fuels and so on, while secondary particles are formed by gas-to-particle conversion in the atmosphere (Pöschl, 2005). Aerosol particles in the atmosphere can have lifetimes of several days, during which they can undergo continuous physical and chemical processing (Rudich et al., 2007). The contribution of secondary organic aerosols (SOA) to PM varies with seasons and locations, but usually accounts for 20%-80% of the measured mass (Hallquist et al., 2009; Kroll and Seinfeld, 2008). Due to the negative impact on public health and the high uncertainty on radiation forcing, more and more attention has been attracted to the SOA related study in recent years, such as yield, chemical composition and optical properties (George and Abbatt, 2010; Jimenez et al., 2009).

It is well-known that SOA formation is related to many aspects, for instance, preexisting inorganic particles. Ammonium sulfate (AS) is considered as one of the most common inorganic seed aerosols in the atmosphere, and one of the most important inorganic compounds in sub-micrometer mixed particles (Robinson et al., 2013; Wang et al., 2011). AS

* Corresponding author.
E-mail: lindu@sdu.edu.cn (L. Du).

https://doi.org/10.1016/j.jes.2020.03.050

Table 1 – Initial experimental conditions of secondary organic aerosol (SOA) formation experiment.

Exp.	Ether	$[Ether]_0$ (ppbV)	$[AS]_0$ (μg/m^3)	$[H_2O_2]_0$ (ppmV)	$[NO_x]_0$ (ppbV)	ΔM_0 (μg/m^3)	Yield (%)
1	MnPE	292	–	1.83	–	5.0	0.5
2	MsBE	339	–	1.84	–	4.4	0.4
3	MnBE	278	–	1.25	–	8.4	0.7
4	EnBE	334	–	1.87	–	9.6	0.8
5	MtBE	314	–	1.99	–	3.0	0.2
6	DnPE	366	–	1.96	–	8.0	0.7
7	MnPE	252	34.4	1.26	–	119.2	11.0
8	MnBE	207	31.2	1.20	–	220.5	27.0
9	MnBE	218	38.7	–	249	–	–
10	MnBE	202	32.2	1.17	110	105.9	10.7

Exp.: experiment; -: the reactant was not added or the concentration was below the detection limit; $[Ether]_0$ and $[H_2O_2]_0$: the initial concentration of ether and H_2O_2, respectively; $[AS]_0$ and $[NO_x]_0$: the stabilized concentrations of seed aerosol and NO_x, respectively; MnPE: methyl *n*-propyl ether; MsBE: methyl *s*-butyl ether; MnBE: methyl *n*-butyl ether; EnBE: ethyl *n*-butyl ether; MtBE: methyl *t*-butyl ether; DnPE: di-*n*-propyl ether; ΔM_0: the net mass concentration of the new particles.

seed aerosol was often used because of its tendency to form approximately spherical seed particles (Meyer et al., 2009). Moreover, the ratio between volatile organic compound (VOC) and NO_x concentrations has been found to be highly influential in SOA formation and many chamber studies employed the value of initial concentration ratio of VOC to NO_x between 4 to 6 (Tsiligiannis et al., 2019; Zhao et al., 2018). This dependence seems to be attributed to differences in the chemistry of organic peroxide radicals (RO_2) (Surratt et al., 2006). In the absence of NO_x (mixing ratio of $NO_x < 1$ ppbV), RO_2 radicals react with HO_2 radicals (the large quantities from the $OH + H_2O_2$ reaction) to form organic hydroperoxides, which have been proven to be an important SOA components of other VOC precursors (Docherty et al., 2005; Johnson et al., 2004). Under high NO_x conditions, peroxide radicals (RO_2) react with NO to form alkoxy radicals (RO), thus reducing the formation of SOA (Loza et al., 2014; Zhang et al., 2014). The fragmentation/decomposition of RO radicals can produce higher volatility substance or form organic nitrate which can suppress the SOA formation (Lim and Ziemann, 2009; Riva et al., 2016).

Although the formation of SOA from gas-phase has been getting great interest in recent years, few related studies have been investigated on ether compounds. Formation of SOA was observed during the ozonolysis of a series of enol ethers and alkyl vinyl ethers (e.g., ethyl, propyl, and *n*-butyl vinyl ether) in the gas phase (Sadezky et al., 2006). For all enol ethers, the measured SOA yields ranged from 2% to 4% (Sadezky et al., 2006). A recent study investigated glycol ethers and related ethers in the presence of NO_x or "NO_x free" conditions. The results showed that the contribution of glycol ethers to anthropogenic SOA was about 1% of the current organic aerosol from mobile sources (Li and Cocker, 2018).

In general, short aliphatic ethers are less volatile and more reactive than alkanes with the same amount of carbons in the oxidation process (Mellouki et al., 2003). Aliphatic ethers also have a wide range of applications, such as fuel additives, alternative fuels, and chemical intermediates (Japar et al., 1990; Semelsberger et al., 2006). For instance, methyl *t*-butyl ether (MtBE) has been widely used as an octane booster and oxygenate additive in gasoline since the late 1970s (Tang et al., 2019). Environmental monitoring data showed that the concentration of MtBE was 3.60 μg/m^3 at a rural mountain site in California (Schade et al., 2002). In order to evaluate the potential capacity of short aliphatic ether to produce SOA under complex pollution conditions, it is necessary to have a better understanding of the atmospheric chemistry of these species.

In this study, six kinds of short chain aliphatic ether were selected, namely methyl *n*-propyl ether (MnPE, >95%, TCI, Japan), methyl *n*-butyl ether (MnBE, >99%, TCI, Japan), methyl *s*-butyl ether (MsBE, >98%, TCI, Japan), methyl *t*-butyl ether (MtBE, >99%, TCI, Japan), ethyl *n*-butyl ether (EnBE, >99%, TCI, Japan), and di-*n*-propyl ether (DnPE, >98%, TCI, Japan). The potential of SOA formation and SOA size distribution for those ethers were investigated using a scanning mobility particle sizer (SMPS) spectrometer. In addition, the effect of NO_x and ammonium sulfate seed on ether SOA yield was discussed. A set of offline analytical techniques was employed to elucidate the detailed chemical composition of SOA from ether oxidation.

1. Materials and methods

1.1. *Smog chamber experiments*

Experiments were conducted in a 1 m^3 Teflon smog chamber at room temperature 295 ± 2 K and atmospheric pressure. The chamber was made of 0.06 mm Teflon film. Details of the facilities were provided by Liu et al. (2019). The chamber was equipped with sixteen ultraviolet lamps (36 W, Philips, Netherlands) with central maximum intensity at 254 nm and sixteen black light (F40T12/BLB, GE, USA) with maximum intensity at 365 nm. The ultraviolet lamp was mainly used to generate OH radicals, which was produced from hydrogen peroxide (H_2O_2, 30% by volume in water, Aladdin, China) photolysis, and the black lamp was mainly used for the photolysis of NO_x. Before each experiment, the smog chamber was flushed with synthetic air by a zero-air gas generator (Model 111-D3N, Thermo Scientific, USA) for at least three hours until the particle number concentration was < 10 particles/cm^3 and volume concentration < 0.01 μm^3/cm^3. The reactant was added with the calibrated micro syringe and flushed into the system with synthetic air. In NO_x free experiments, NO (510 ppmV NO in N_2, Qingdao Yuyang Special Gas, China) or NO_2 (507.6 ppmV NO_2 in N_2, Qingdao Yuyang Special Gas, China) was not added into the chamber and concentrations of NO_x were less than 1 ppbV. The initial NO_x concentration of 110 to 249 ppbV was obtained by adding NO_2 into the chamber from the premixed cylinder. AS (98 vol.%, Adamas-beta, China) seed aerosol was introduced into the chamber via atomization of 0.15 mol/L aqueous AS solution and an electrospray aerosol atomizer (Model 3076, TSI, USA) was employed. After completing the injection, the seed aerosols were stabilized in the chamber for approximately 20 min. The initial experimental conditions are listed in Table 1. The initial concentration of ether ($[ether]_0$) and H_2O_2 ($[H_2O_2]_0$) were around 202–366 ppbV and 1.17–1.99

ppmV, respectively. The initial seed mass concentration in the chamber ranged from 31.2 to 38.7 μg/cm^3.

The concentrations of ethers were measured using a gas chromatograph-flame ionization detector (GC-FID 7890B, Agilent Technologies, USA) equipped a capillary column (DB-624, Agilent Technologies, USA, 30 m length × 1.8 μm film thickness × 0.32 mm inner diameter). The real-time concentrations of NO-NO_2-NO_x and O_3 were measured by NO_x analyzer (Model 42i, Thermo Scientific, USA) and O_3 analyzer (Model 49i, Thermo Scientific, USA), respectively. A humidity/temperature measuring instrument (Model 645, Testo, Germany) shows the measurement parameters of relative humidity and temperature before and after the experiment.

A scanning mobility particle sizer (SMPS, Model 3983, TSI, USA), which consists of electrostatic classifier (Model 3082, TSI, USA) and differential mobility analyzer (Model 3081, TSI, USA), with a condensation particle counter (Model 3776, TSI, USA) were used to measure the size distributions and number concentrations of the newly formed particles. The aerosol sampling rate and sheath gas rate were 1.5 and 15.0 L/min, respectively. The scanning range of particle size was from 13.8 to 723.4 nm with 5 min for each sample (including 180 sec scanning time). Assuming the aerosol density is 1.0 g/cm^3, the particle volume is converted to mass concentration. Size data of SOA were recorded and analyzed by the Aerosol Instrument Manager 10.2 software. The SOA yield (Y) was calculated according to the following equation (Odum et al., 1996):

$$Y = \frac{M_0}{\Delta VOC} \times 100\% \quad (1)$$

where M_0 is the peak mass of SOA produced and ΔVOC is the amount of the precursor VOC consumed at peak SOA mass (both expressed in units of μg/m^3).

1.2. SOA chemical composition

The particles were collected on the aluminum foil (diameter 25 mm) by a low-pressure impactor (DLPI+, Dekati, Finland) in the range of 16 nm–10 μm. The operating principle of this low-pressure impactor is based on inertial size classification and gravimetric or chemical analysis of the collected, size classified particle samples. A Fourier transform infrared spectrometer (FTIR, Vertex 70, Bruker, USA) equipped with an attenuated total reflection accessory (ATR) and a liquid-nitrogen-cooled HgCdTe (MCT) detector was employed for chemical composition measurements. The aluminum foil sample was put in the ATR-FTIR sample holder to analysis the basic functional groups for the formed SOA particles. ATR-FTIR was equipped with a diamond crystal and operated at the resolution of 4 cm^{-1} with 128 scans. Each ATR-FTIR analysis uses the same settings to collect background spectra and subtract them from the sample spectra.

Because the low-pressure impactor divides the particles into 14 size classes, the collection efficiency was not significantly high. Polytetrafluoroethylene (PTFE) filter was also used to collect SOA particles. The gas in the chamber was pumped at a rate of 15 standard liters per minute through PTFE filters. The collected particles were extracted by placing the filter on the bottom of the beaker. SOA materials were dissolved in methanol (≥99.9%, Aladdin, China) for 15–20 min. A fresh solution was prepared for the experiment and used immediately. To have an analysis reference, we used the same procedure and analyzed with a blank filter. No significant chemical artifacts or contaminants were observed.

Gas chromatography–mass spectrometry (GC–MS, 5977D MSD, Agilent Technologies, USA) was also used for the analysis of SOA chemical composition produced from the photooxidation reaction. The sample was rapidly heated to 523 K and injected the sample into the HP-5MS capillary column (30 m length × 0.50 μm film thickness × 0.25 mm inner diameter, Agilent Technologies, USA). The column oven temperature was initially kept at 303 K for 1 min and then heated to 373 K at a rate of 5 K/min, and finally, it raised to 523 at a rate of 10 K/min.

1.3. SOA optical properties

The SOA optical properties were analyzed using an ultraviolet and visible (UV–Vis) spectrometer (P9, Mapada, China) and a fluorescence spectrophotometer (F-320, Tianjin Gangdong, China). The UV–Vis spectrometer is a dual-beam optical system with tungsten lamp and deuterium lamp as light sources. The sample was drawn into the 4 mL cuvette and then detected in the wavelength range of 200–700 nm. A reference of methanol solvent was used for the sample measurement. The absorption coefficient (α) was measured base-10 absorbance value (A_{10}), then the value was converted into base-e solution absorption coefficients by normalizing to the cell path length (l) (Aiona et al., 2018).

$$\alpha(\lambda) = \frac{A_{10}(\lambda) \times \ln(10)}{l} \quad (2)$$

After measurements by UV–Vis spectrometer, the cuvette was transferred into a fluorescence spectrophotometer. Three-dimensional excitation-emission matrix (EEM) spectra of SOA extracts were obtained. The excitation and emission wavelength are between 200 and 760 nm.

2. Results and discussion

2.1. SOA size distributions

Time-series of the particle size distribution and number concentration in the seedless experiments are presented in Fig. 1. Before the light was turned on, there was no obvious particle in all panels, which indicated that the particle formation could not occur under the dark conditions. All the panels showed the same pattern and the SOA distribution of all the experiments showed a single aerosol mode during the whole time-series. The dotted line represents the time of light turning on and off. The initial time represented the point when the SMPS connected after all reactants were injected into the system.

Taking experiment 1 (Exp. 1 in Table 1) as an example, the variation of particle size distribution and number concentration in the whole experiment process was shown for MnPE reaction with OH radicals (Fig. 1). Formation of the detectable particle was observed after 10 min when the system exposed to light. The particle concentration was approximately 4.59 × 10^4 particles/cm^3 and the particle mode diameter was 18 nm at that moment. The maximum total particle concentration of 1.96 × 10^5 particles/cm^3 reached at mode diameters of around 29 nm after 25 min. About 140 min later, at the end of the reaction, the size distribution of SOA was around 41 nm, and the total particle concentration was 8.74 × 10^4 particle/cm^3. The results of size distribution and number concentration in several other systems were similar to that of MnPE reaction with OH radicals. The maximum number concentration was around 2.12 × 10^5, 4.67 × 10^5, 1.98 × 10^5, 0.74 × 10^5 and 7.31 × 10^5 particle/cm^3 for MsBE, MnBE, EnBE, MtBE and DnPE, respectively. The stable particle diameter for each experiment was about 38, 33, 47, 50 and 70 nm for MsBE, MnBE, EnBE, MtBE and DnPE, respectively. The same process was also observed in the ozonolysis of alkyl vinyl ether system. For instance, ethyl vinyl ether SOA appeared as a single aerosol mode and a maximum total particle concentration of 5 × 10^5 to 1 × 10^6 particle/cm^3 was reached after 55 min at mode diameters around 20 nm (Sadezky et al., 2006). The final SOA size distribution of ethyl vinyl ether stabled at mode

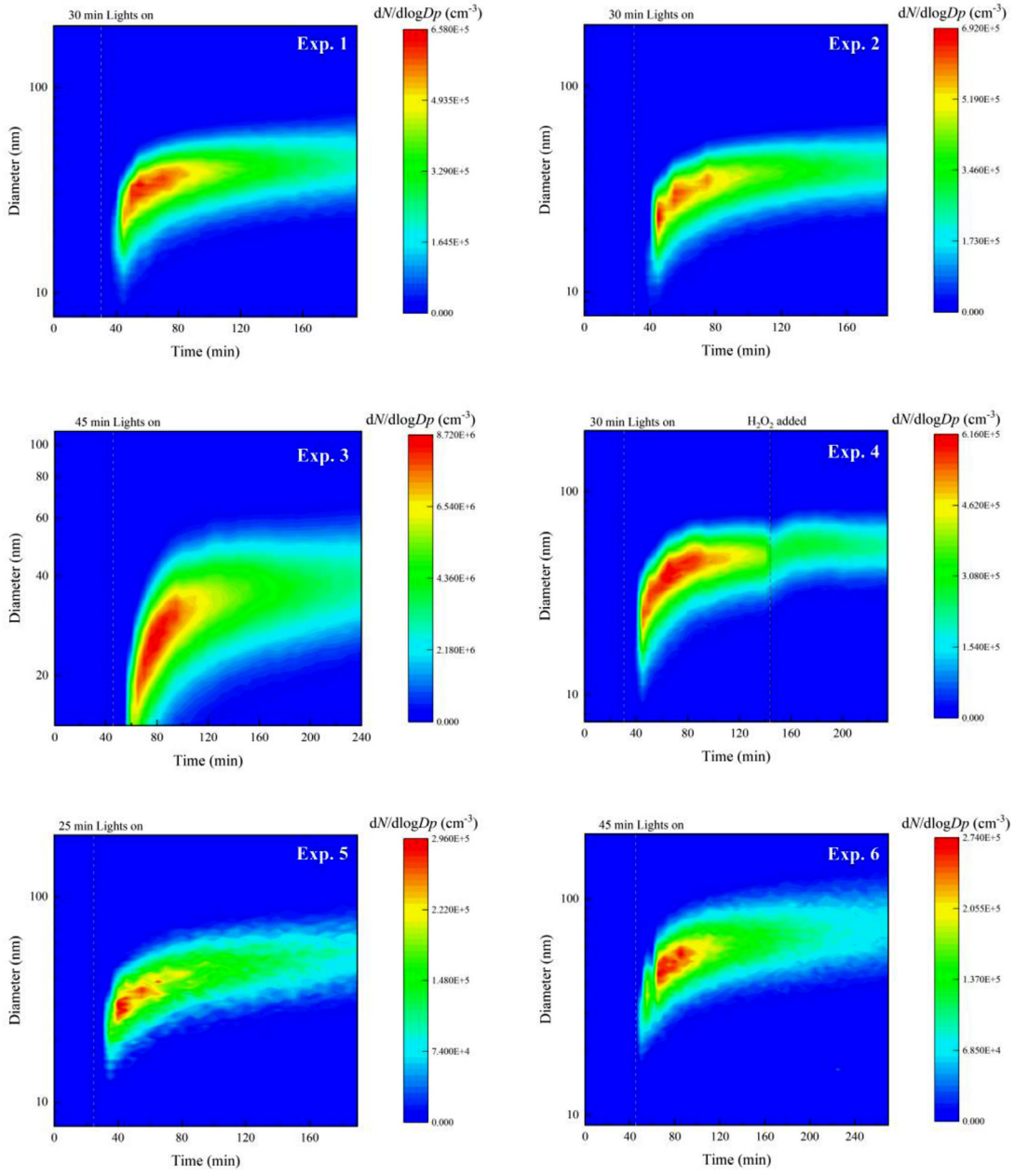

Fig. 1 – Time-series of the particle size distributions and number concentrations for the six aliphatic ethers secondary organic aerosol (SOA) under seedless experiments (Exps. 1–6). N: the number of particles in the range (total concentration); dlogDp: the difference in the log of the channel width.

diameters around 50 nm and the total particle concentration was 1×10^5 particle/cm^3 (Sadezky et al., 2006).

MnPE ($CH_3OCH_2CH_2CH_3$) with only four carbon atoms and EnBE/DnPE ($CH_3CH_2OCH_2CH_2CH_2CH_3$/$CH_3CH_2CH_2OCH_2CH_2CH_3$) with just six carbon atoms are the significant small compound for aerosol production during atmospheric degradation. Previous study has indicated that seven or more carbon atoms were needed to initiate SOA formation (Seinfeld and Pankow, 2003). Here, we demonstrated that the formation of SOA has been observed during the gas-phase photooxidation of a series of short aliphatic ethers. The oligomers might be produced by the photooxidation of gas-phase products and contribute to SOA formation to a large extent. During the previous study, the oligomer with structure, -$[CH_2$-O-O$]_n$-, was proposed during ozonolysis of alkyl vinyl ether (Sadezky et al., 2006).

The detailed time evolution of particle size distribution and number concentration for Exps. 7 and 8 are illustrated in Appendix A Fig. S1 in supplementary data. In the presence of seed particles, the mode diameter of MnPE SOA and MnBE SOA stabilized at 54 and 65 nm at the end of the reaction, which were significantly larger than those without seed conditions. When the seed particles existed, the particle diameter increased due to condensation of gaseous reaction products onto the particle surface and coagulation (Sadezky et al., 2006). For some species, such as acetone and acetylene, it has been demonstrated that SOA cannot be generated via homogeneous reaction in the photooxidation system unless the seed particles were added in the system (Ge et al., 2017a; Volkamer et al., 2009). When comparing the initial particle number concentration and total reaction time between seed and seedless experiments, seed aerosols can promote the

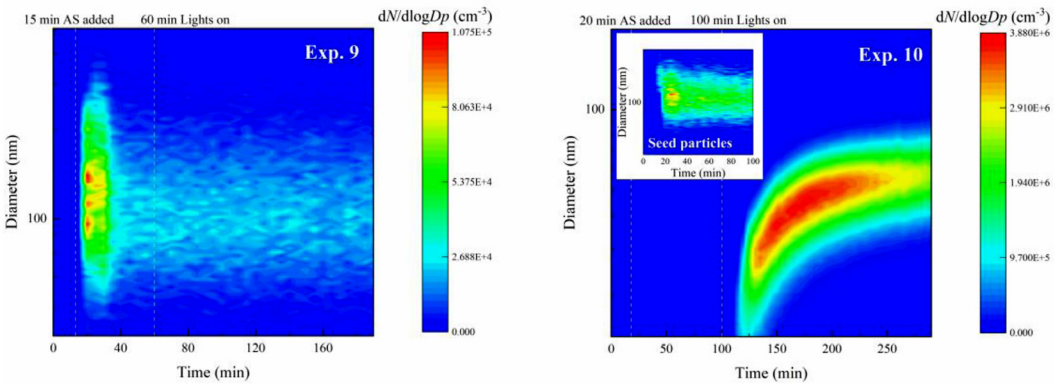

Fig. 2 – Time-series of the particle size distributions and number concentrations for methyl *n*-butyl ether (MnBE) SOA in experiment 9 (Exp. 9) and experiment 10 (Exp. 10). The inset in the right panel stands for the seed particle size distribution and number concentration.

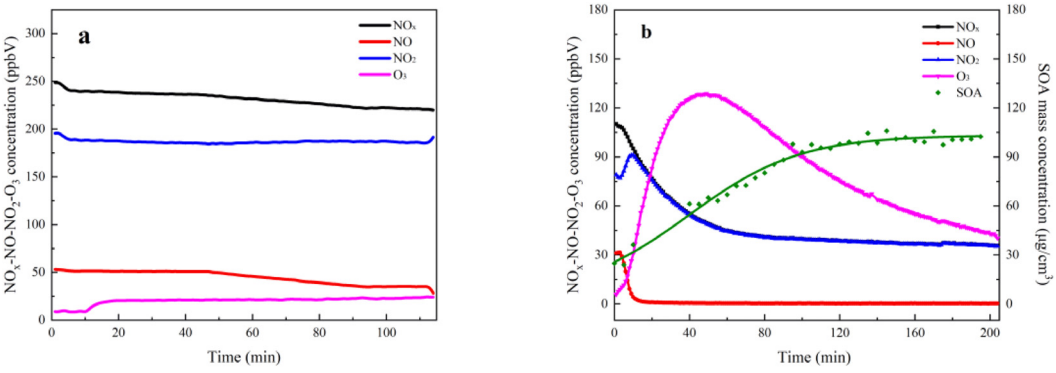

Fig. 3 – Time-series of the NO_x-NO-NO_2-O_3 and SOA mass concentration for (a) Experiment 9 and (b) Experiment 10.

growth rates of SOA formation at the start of the reaction and inhibits its formation rate with the extension of reaction time.

The detailed time-series of particle size distribution and number concentration for Exps. 9 and 10 are illustrated in Fig. 2. The two sets of experiments were conducted under NO_x condition. The SOA formation events could be observed for all experiments except Exp. 9. The temporal evolution of NO_x-NO_2-NO-O_3 concentration of Exp. 9 is illustrated in Fig. 3a. The concentration for each species remained almost unchanged throughout the whole experiment. However, SOA can be formed in the system of propylene-NO_2-NaCl oxidation (Ge et al., 2017b). Unlike the alkenes, ether did not react with O_3 and Criegee intermediates cannot be formed from the ether-NO_x system. Criegee intermediate played a key role in the formation of oligomeric hydroperoxides as a chain unit, which could be accounted for the SOA formation (Sakamoto et al., 2013).

Different from Exp. 9, H_2O_2 was added in Exp. 10. In this case, the particle formation could be detected. The temporal evolution of NO_x-NO_2-NO-O_3 concentration and SOA mass concentration in Exp. 10 is displayed in Fig. 3b. Furthermore, the NO_x concentration gradually decreased with the increase of the SOA mass concentration, which means that NOx participated in the SOA formation. It is generally accepted that the branching ratio of RO_2 reaction with NO_x and HO_2 was determined by the NO_x level (Ng et al., 2007). The initial ether/NO_x molar ratio was ~0.5 in Exp. 10, and RO_2 reaction with NO was the main reason for the decrease of NO_x concentration. Oxygen and NO in the ground state are usually produced by photolysis of NO_2 in existing systems of NO_x (Calvert et al., 2002; Wyche et al., 2009). Under the experimental condition, O_3 and NO_3 radicals played a minor role in the initial oxidation of ether, because they form only once [NO] near zero, by which time most of the ether was consumed (Hallquist et al., 2009).

2.2. *SOA yield*

Some laboratory and field works showed that the realistic SOA density is 1.2–1.4 g/cm^3 (Alfarra et al., 2006), while for the individual substance, the actual SOA density of photooxidation is about 1 g/cm^3. In addition, it is generally believed that 1 g/cm^3 SOA density can assume to convert organic aerosol volume concentration to mass concentration in previous studies (Cocker Iii et al., 2001a, 2001b; Lu et al., 2009; Odum et al., 1996; Song et al., 2005, 2007). The measured average particle loss rate was applied to the entire experiment to correct particle-wall deposition, and SOA mass was corrected as the wall loss by fitting the first-order loss rate calculated by the particle concentration attenuation at the end of each experiment. Considering the particle size distribution in each experiment was around 10–200 nm, the dependence of particle-wall loss rate on particle size was not strong. Thus, a single decay rate coefficient could allow for the overall particle-wall loss to be characterized (Nah et al., 2017).

Total aerosol mass concentration versus reaction time in the no seed experiments are illustrated in Appendix A Fig. S2. A maximum SOA mass concentration reached to about 8.4 μg/m^3 in these experiments. SOA yields for the Exps. 1–6 were 0.5%, 0.4%, 0.7%, 0.8%, 0.2% and 0.7%, respectively. Particle formation was detected in all six photooxidation experiments. The mass concentration for six experiments

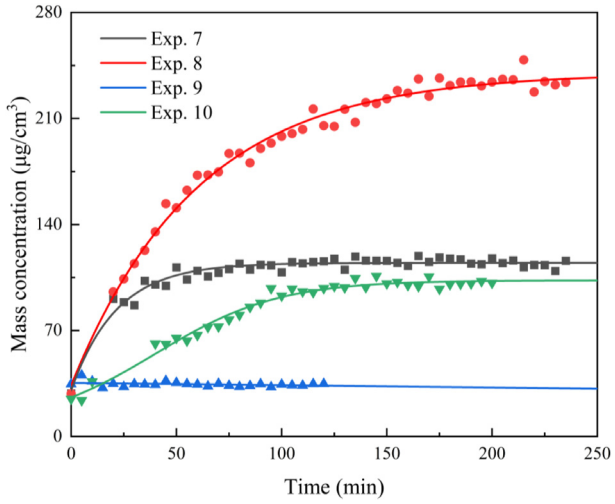

Fig. 4 – Total aerosol mass concentration versus reaction time for the seed experiments (Exps. 7–10).

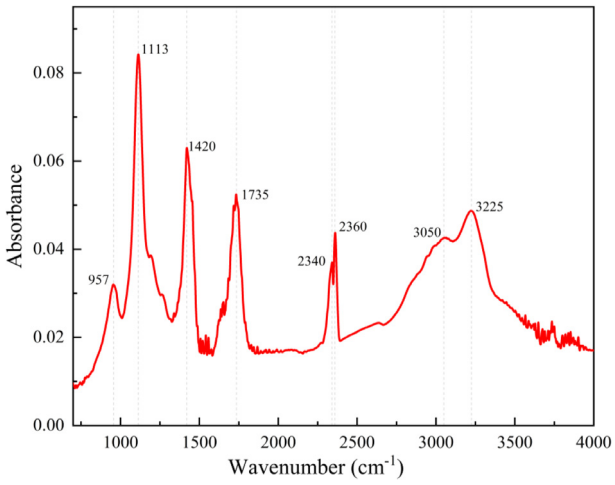

Fig. 5 – Infrared spectrum of MnBE SOA under seed and NO_x condition.

was less than 10 μg/m^3 and the SOA yields were less than 1%. In previous studies, the SOA yield of ozonolysis of iso-butyl vinyl ether was 0.9% when excessive cyclohexane was used as OH scavenger (Sadezky et al., 2006). For the ozonolysis of methyl vinyl ether, the SOA yield was also small, around 0.66% (Klotz et al., 2004). The small amount of SOA, 4.4–10.3 μg/m^3, was formed from ethylene glycol diethyl ether under the H_2O_2-only condition (Li and Cocker, 2018). Those results demonstrated that typical yield for the no seed ozonolysis or photooxidation experiment could be very small.

Total aerosol mass concentration versus reaction time in the seed experiments are illustrated in Fig. 4. For the seeded experiments, SOA mass concentrations were obtained by subtracting the initial seed aerosol mass concentrations. The corrected maximum mass concentration in Exps. 7 and 8 were 119.2 and 220.5 μg/m^3, respectively, significantly higher than the observed values of seedless experiments. These results were consistent with the previous studies, when SOA yields of ethylbenzene and *m*-xylene were enhanced in the presence of $(NH_4)_2SO_4$ seed aerosol (Huang et al., 2016; Kroll et al., 2007; Lu et al., 2009). On one hand, the increased aerosol mass was contributed to larger surface area provided by seed particles. More surface area means more condensation of semi- or low-volatile products (Ge et al., 2017b). On the other hand, AS particles may provide more reaction sites for heterogeneous reactions (Czoschke et al., 2003). The vapor pressures of these heterogeneous reaction products are much lower than that of the parent aldehydes, which mainly exists in the particle phase. The aldehyde distribution between the gas and particle phase is reconstructed by equilibrium distribution (Czoschke et al., 2003). At the same time, AS seed aerosol may also initiate the ammonium catalyzed heterogeneous reactions, such as hydration and polymerization of aldehydes initiated by OH radical (George et al., 2015).

In Exp. 10, the high-NO_x concentration was achieved by the addition of substantial NO_x (249 ppbV NO_x) into the chamber, leading to ether/NO_x molar ratios of ~0.5 (Ng et al., 2007). Compared with Exp. 8, the SOA yield significantly decreased in Exp. 10. The yield of SOA decreases with the increase of NO_x, which may due to the formation of more volatile products, such as organic nitrates, under high NO_x conditions (Presto et al., 2005). The suppressing effect of NO_x was largely attributed to the effect of NO_x on OH concentration in the SOA from β-pinene oxidation (Sarrafzadeh et al., 2016). In addition to the effect of NO_x on SOA yield, high NO_x also suppresses the new particle formation, thereby reducing the condensational sink present in the high-NO_x experiments (Sarrafzadeh et al., 2016; Zhao et al., 2018). However, some results are in contrast with our finding (Han et al., 2016; Presto et al., 2005; Stirnweis et al., 2017). Those studies reported much lower SOA yield at high NO_x than at low NO_x condition in the presence of seed particles. This difference could probably be attributed to the different reaction condition such as oxidation pathways, organic aerosol loading, and OH concentrations.

2.3. *SOA chemical composition*

In the gas-phase, the general initial step of OH radical reaction with ethers was the abstraction of H atom from the C-H bond (Mellouki et al., 2003). The initial carbon-centered radicals react with O_2 to form peroxide radicals, which react with other peroxide radicals by themselves or cross-react, mainly to form alkoxy radicals (Mellouki et al., 2003; Zhu et al., 2017). The final gas products were formed subsequently through further decomposition pathway. Some carbonyl products were identified for the reaction of MnBE with OH radicals, such as 2-butanone and acetaldehyde (Zhu et al., 2019).

The chemical composition of SOA particles generated by MnBE photooxidation in the presence and absence of NO_x was analyzed by ATR-FTIR, and their IR spectra are shown in Fig. 5 and Appendix A Fig. S3, respectively. No big difference was observed between the two spectra with or without NO_x. To some extent, this indicates that the presence or absence of NO_x does not change the main chemical composition of the SOA particles. Certain amounts of organic nitrates were expected to be formed considering the existence of NO_x in the system. However, there is no significant evidence showing the formation of organic nitrates in the measured IR spectra, possibly due to their limited abundance in the SOA particles. In Fig. 5, the characteristic absorption features of carboxylic acids locate at 2500–3300 cm^{-1} (O-H stretching) and ~1113 cm^{-1} (C-O stretching) in the spectrum. In general, these species were produced by the reaction between RO_2 and HO_2 (Czoschke et al., 2003; Miyoshi et al., 1994). The previous result showed that there is O-H deformation vibration near 957 cm^{-1} and C=O tension at 1735 cm^{-1} (Liu et al., 2015). As mentioned above, there were some carbonyl species existed in the gas phase. Further oxidation or the gas-particle phase partition may both lead to the existence of the species in the particle phase. There were very weak band at 1280 and 1640 cm^{-1}, which may be related to the symmetric stretching and asym-

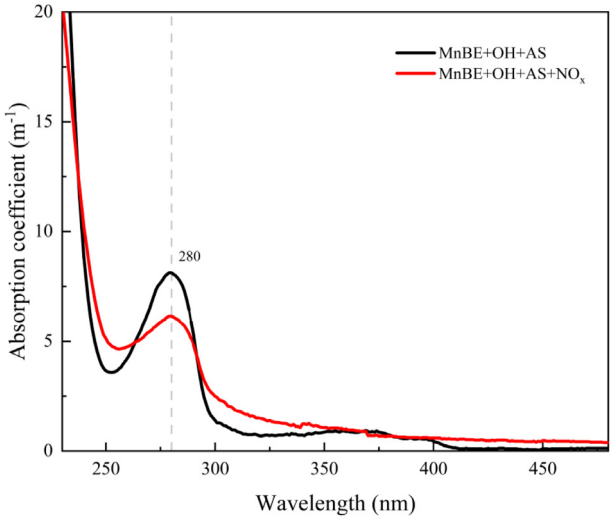

Fig. 6 – Ultraviolet-visible absorption spectra of MnBE SOA under NO_x free and NO_x contained condition. AS: ammonium sulfate; OH: hydroxyl radical.

metric stretching of NO_2 in $RONO_2$ (Bruns et al., 2010). Under normal system containing NO_x, the ether hydroxy peroxide radicals react predominantly with NO. At the same time, they may also react with NO_2 to form peroxide nitrates (Ng et al., 2007). However, due to their thermal instability, these species may not be important for the formation of ether SOA (Surratt et al., 2006). Nitrogen-containing organic compounds are affected not only by NO_x, but also by ammonium salts. Schiff base and/or Mannich reaction between ammonium salts and carbonyl functional groups in particles can also form organonitrogen compounds (Liu et al., 2015). In the previous study, 1H-imidazole-2-carboxaldehyde was identified as one C-N product in the glyoxal SOA system, and this C-N compound had a significant band at 1420 cm^{-1} (Galloway et al., 2009).

SOA chemical composition was also analyzed by GC-MS. 2,2-Dimethyl butane and 1,3,5-trioxane were detected as particle-phase products. The mass spectra of detected products are shown in Appendix A Fig. S4. Combined the FTIR spectrum with GC-MS data, it is further recognized that there are many oxidation products, and the concentration of each product is relatively low. In the previous studies, organic sulfate compounds were identified in acetone-oxidized SOA when AS seeds existed in the system (Ge et al., 2017b). The organic sulfates could be formed by the reaction of organic compounds with sulfuric acid or sulfate ions under acidic conditions (Ge et al., 2017b). However, organic sulfate was not identified in our experiment. Although it has been established that OH-initiated oxidation of ethers leads to SOA formation, a detailed understanding of the chemical reaction pathways leading to the production of ether SOA needs to be studied in the future.

2.4. *SOA optical properties*

The absorption property for the extracting solutions of MnBE SOA was measured by a dual-beam UV–Vis spectrometer. The absorption spectra under NO_x contained (red line) and NO_x free (black line) condition is shown in Fig. 6. Maximum absorption occurred at 280 nm and slight absorption occurred in the UV region (300–400 nm). Absorption of visible light occurs only in the system containing NO_x. Previous study has shown that the photooxidation of aromatic compounds under high NO_x conditions is the process of nitrophenol formation, and the contribution of nitrophenol to the absorption coefficient is dominant (Liu et al., 2016). In addition to nitrophenols, quinones in naphthalene SOA could also absorb in the visible region (Aiona et al., 2018). Although the precursor in the experiments are ethers, the UV–Vis absorption spectra of MnBE SOA suggested that AS seed directly participated in the generation of SOA or some organic amine species were produced with particle-phase products (intermediates). The reaction of carbonyl compound with ammonium sulfate in aqueous-phase can form some light-absorbing species (Powelson et al., 2014). Some studies further demonstrated that AS seed aerosol form ammonium ion (NH_4^+) by absorbing water from its outer organic layer coating and ammonium ion could react with carbonyl compounds, such as glyoxal and methylglyoxal, to from imidazole species (Kampf et al., 2012; Nozière et al., 2009; Yu et al., 2011). The high mass concentrations of AS seed aerosol can promote the formation of imidazole compounds in aged ethylbenzene SOA (Huang et al., 2016; Kampf et al., 2012). FTIR spectra also showed that there were some carbonyl compounds formed. We speculated that the above conclusion maybe only for the fresh SOA. If the ether SOA undergoes further oxidation and aging, the absorption of aerosol may change. Here, we took the first step for exploring the light-absorbing property with the ether SOA.

The excitation-emission property for the MnBE SOA was also measured by a fluorescence spectrophotometer. The EEM data for MnBE SOA generated with or without NO_x are shown in Fig. 7, with panel **a** and **b** representing the experiment without NO_x and with NO_x, respectively. In Fig. 7a and b, MnBE SOA displayed the same distinct peak at excitation/emission (ex/em) = 470 nm/480 nm. But for the NO_x contained sample, there were broad regions around 400 nm/410 nm and 350 nm/400–500 nm where the fluorescence increased. These results also indicated that NO_x can involve in the particle-phase. Increased fluorescence may also indicate the formation of new fluorophores or the loss of quenching compounds/moieties (Lee et al., 2014). Combined the EEM and UV–Vis spectra, the fresh MnBE SOA exhibited the absorption and fluorophores properties in some wavelength range and NO_x has a small effect on the optical properties of MnBE SOA.

2.5. *Atmospheric implication*

According to the gas-phase rate constants and OH average global concentration, the calculated atmospheric lifetimes for MnPE, MsBE, MtBE, MnBE, EnBE, and DnPE were 28, 27, 85, 19, 13 and 14 h, respectively (Nelson et al., 1990; Semadeni et al., 1993; Smith et al., 1991; Zhu et al., 2019). Those previous studies have indicated that the atmospheric degradation of short chain aliphatic ethers is mainly due to their reactions with OH radicals in the gas-phase. On the basis of these studies, we further demonstrated that SOA can be produced by the reaction of ether with OH radicals even without seeds and NO_x. Although the stable mode diameters in our experiment are around 50 nm, the significant Brownian motion will exist under this scale. Due to condensation of gaseous or semi/low volatile species and condensation with other aerosol particles, the particle size of these nanoscale aerosols can easily increase in the ambient atmosphere.

The concentrations of NO_x in our experiments are several times higher than that in the ambient atmosphere. The observed data indicated the annual population-weighted-average values in China was approximately 34.1–21.9 $\mu g/m^3$ for NO_2 during 2014–2016, while during the winter polluted days with NO_2 concentration even above 100 $\mu g/m^3$ (53 ppbV) were also observed in Beijing-Tianjin-Hebei and Yangtze River Delta area (Song et al., 2017). Recent online observation showed that water-soluble inorganic ions accounted for ~52.2% of the $PM_{2.5}$ mass in the Yangtze River Delta, of which sulfate dominated in wet haze periods and nitrate dominated in other periods (Ye et al., 2019). The effects of

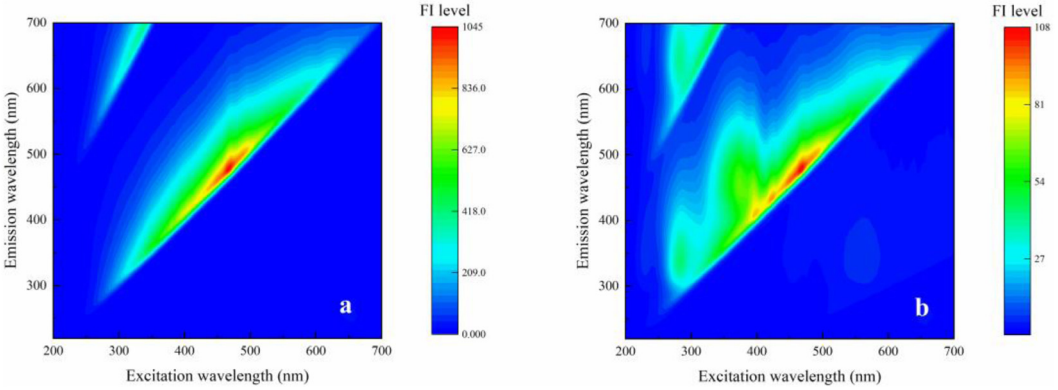

Fig. 7 – Excitation-emission matrix (EEM) plots for MnBE SOA with seed particles under (a) NO_x free and (b) NO_x contained condition. FI: fluorescence intensity.

high concentration AS aerosols in the ambient atmosphere will still be widespread, and the incidence of AS effects may be higher, due to the low mass loading of organic aerosols.

The obtained optical properties indicated that when ethers are released into the atmosphere, the ether SOA absorbs light in the UV–Vis region. As light absorbing carbonaceous aerosols, ether SOA could have a significant impact on the Earth's radiative balance. Since different organic aerosol have different interactions with radiation, the large variability of ether SOA optical properties at the source, and its evolution after atmospheric transport, mixing and aging needs to be well characterized to assess those impacts on climate in the future.

3. Conclusions

In the present work, a series of photochemical oxidation experiments of different ethers were studied in a 1 m^3 smog chamber. The detectable particles could be measured for all the seedless experiments. The mode diameter of different ether SOA systems was stable at around 40–70 nm under seedless and NO_x-free condition. The strong increase in the formation of SOA was observed in the experiments with AS seed particles which were accompanied by enhancement the particle size distribution, mass concentration, and SOA yield. AS particles can prove that semi-volatility products not only have significant larger condensation surface, but also can induce or provide more heterogeneous reaction sites. There were no particles generated in the ether-seed-NO_x system and SOA yield decreased when the system under the high-NO_x condition. We also emphasize that the largest absorption peak is at 280 nm and there exists slightly absorption during the 300–400 nm region for the fresh MnBE SOA. The fluorescence excitation-emission matrices display the distinct peak at ex/em = 470 nm/480 nm. NO_x has a slight effect on the optical properties of MnBE SOA. These results may be useful for SOA formation modeling, especially for air quality simulation modeling in developing cities with serious PM pollution. At the same time, the detailed formation mechanism of particle-phase products and the optical properties with the aging of SOA in the atmosphere need to be further studied.

Declaration of competing interest

The authors declare that they have no known competing financial interests or personal relationships that could have appeared to influence the work reported in this paper.

Acknowledgments

This work was supported by the National Natural Science Foundation of China (No. 91644214), the Shandong Natural Science Fund for Distinguished Young Scholars (No. JQ201705), the Youth Innovation Program of Universities in Shandong Province (No. 2019KJD007), and the Fundamental Research Fund of Shandong University (No. 2020QNQT012).

Appendix A. Supplementary data

Supplementary material associated with this article can be found in the online version at doi:10.1016/j.jes.2020.03.050.

REFERENCES

Aiona, P.K., Luek, J.L., Timko, S.A., Powers, L.C., Gonsior, M., Nizkorodov, S.A., 2018. Effect of photolysis on absorption and fluorescence spectra of light-absorbing secondary organic aerosols. ACS Earth Space Chem. 2, 235–245.

Alfarra, M.R., Paulsen, D., Gysel, M., Garforth, A.A., Dommen, J., Prévôt, A.S.H., et al., 2006. A mass spectrometric study of secondary organic aerosols formed from the photooxidation of anthropogenic and biogenic precursors in a reaction chamber. Atmos. Chem. Phys. 6, 5279–5293.

Bruns, E.A., Perraud, V., Zelenyuk, A., Ezell, M.J., Johnson, S.N., Yu, Y., et al., 2010. Comparison of FTIR and particle mass spectrometry for the measurement of particulate organic nitrates. Environ. Sci. Technol. 44, 1056–1061.

Calvert, J.G., Atkinson, R., Becker, K.H., Kamens, R.M., Seinfeld, J.H., Wallington, T.H., et al., 2002. The Mechanisms of Atmospheric Oxidation of the Aromatic Hydrocarbons. Oxford University Press.

Cocker Iii, D.R., Clegg, S.L., Flagan, R.C., Seinfeld, J.H., 2001a. The effect of water on gas–particle partitioning of secondary organic aerosol. Part I: α-pinene/ozone system. Atmos. Environ. 35, 6049–6072.

Cocker Iii, D.R., Mader, B.T., Kalberer, M., Flagan, R.C., Seinfeld, J.H., 2001b. The effect of water on gas–particle partitioning of secondary organic aerosol: II. m-xylene and 1,3,5-trimethylbenzene photooxidation systems. Atmos. Environ. 35, 6073–6085.

Czoschke, N.M., Jang, M., Kamens, R.M., 2003. Effect of acidic seed on biogenic secondary organic aerosol growth. Atmos. Environ. 37, 4287–4299.

Docherty, K.S., Wu, W., Lim, Y.B., Ziemann, P.J., 2005. Contributions of organic peroxides to secondary aerosol formed from reactions of monoterpenes with O_3. Environ. Sci. Technol. 39, 4049–4059.

Galloway, M.M., Chhabra, P.S., Chan, A.W.H., Surratt, J.D., Flagan, R.C., Seinfeld, J.H., et al., 2009. Glyoxal uptake on ammonium sulphate seed aerosol: reaction products and reversibility of uptake under dark and irradiated conditions. Atmos. Chem. Phys. 9, 3331–3345.

Ge, S., Xu, Y., Jia, L., 2017a. Effects of inorganic seeds on secondary organic aerosol formation from photochemical oxidation of acetone in a chamber. Atmos. Environ. 170, 205–215.

Ge, S., Xu, Y., Jia, L., 2017b. Secondary organic aerosol formation from propylene irradiations in a chamber study. Atmos. Environ. 157, 146–155.

George, C., Ammann, M., D'Anna, B., Donaldson, D.J., Nizkorodov, S.A., 2015. Heterogeneous photochemistry in the atmosphere. Chem. Rev. 115, 4218–4258.
George, I.J., Abbatt, J.P.D., 2010. Heterogeneous oxidation of atmospheric aerosol particles by gas-phase radicals. Nat. Chem. 2, 713–722.
Hallquist, M., Wenger, J.C., Baltensperger, U., Rudich, Y., Simpson, D., Claeys, M., et al., 2009. The formation, properties and impact of secondary organic aerosol: current and emerging issues. Atmos. Chem. Phys. 9, 5155–5236.
Han, Y., Stroud, C.A., Liggio, J., Li, S.M., 2016. The effect of particle acidity on secondary organic aerosol formation from α-pinene photooxidation under atmospherically relevant conditions. Atmos. Chem. Phys. 16, 13929–13944.
Huang, M., Zhang, J., Cai, S., Liao, Y., Zhao, W., Hu, C., et al., 2016. Characterization of particulate products for aging of ethylbenzene secondary organic aerosol in the presence of ammonium sulfate seed aerosol. J. Environ. Sci. 47, 219–229.
Japar, S., Wallington, T., Richert, J., Ball, J., 1990. The atmospheric chemistry of oxygenated fuel additives: t-butyl alcohol, dimethyl ether, and methyl t-butyl ether. Int. J. Chem. Kinet. 22, 1257–1269.
Jimenez, J.L., Canagaratna, M.R., Donahue, N.M., Prevot, A.S.H., Zhang, Q., Kroll, J.H., et al., 2009. Evolution of organic aerosols in the atmosphere. Science 326, 1525–1529.
Johnson, D., Jenkin, M.E., Wirtz, K., Martin-Reviejo, M., 2004. Simulating the formation of secondary organic aerosol from the photooxidation of toluene. Environ. Chem. 1, 150–165.
Kampf, C.J., Jakob, R., Hoffmann, T., 2012. Identification and characterization of aging products in the glyoxal/ammonium sulfate system - implications for light-absorbing material in atmospheric aerosols. Atmos. Chem. Phys. 12, 6323–6333.
Klotz, B., Barnes, I., Imamura, T., 2004. Product study of the gas-phase reactions of O_3, OH and NO_3 radicals with methyl vinyl ether. Phys. Chem. Chem. Phys. 6, 1725–1734.
Kroll, J.H., Chan, A.W.H., Ng, N.L., Flagan, R.C., Seinfeld, J.H., 2007. Reactions of semivolatile organics and their effects on secondary organic aerosol formation. Environ. Sci. Technol. 41, 3545–3550.
Kroll, J.H., Seinfeld, J.H., 2008. Chemistry of secondary organic aerosol: Formation and evolution of low-volatility organics in the atmosphere. Atmos. Environ. 42, 3593–3624.
Lee, H.J., Aiona, P.K., Laskin, A., Laskin, J., Nizkorodov, S.A., 2014. Effect of solar radiation on the optical properties and molecular composition of laboratory proxies of atmospheric brown carbon. Environ. Sci. Technol. 48, 10217–10226.
Li, L., Cocker, D.R., 2018. Molecular structure impacts on secondary organic aerosol formation from glycol ethers. Atmos. Environ. 180, 206–215.
Lim, Y.B., Ziemann, P.J., 2009. Effects of molecular structure on aerosol yields from OH radical-initiated reactions of linear, branched, and cyclic alkanes in the presence of NO_x. Environ. Sci. Technol. 43, 2328–2334.
Liu, J., Lin, P., Laskin, A., Laskin, J., Kathmann, S.M., Wise, M., et al., 2016. Optical properties and aging of light-absorbing secondary organic aerosol. Atmos. Chem. Phys. 16, 12815–12827.
Liu, S., Tsona, N.T., Zhang, Q., Jia, L., Xu, Y., Du, L., 2019. Influence of relative humidity on cyclohexene SOA formation from OH photooxidation. Chemosphere 231, 478–486.
Liu, Y., Liggio, J., Staebler, R., Li, S.M., 2015. Reactive uptake of ammonia to secondary organic aerosols: kinetics of organonitrogen formation. Atmos. Chem. Phys. 15, 13569–13584.
Loza, C.L., Craven, J.S., Yee, L.D., Coggon, M.M., Schwantes, R.H., Shiraiwa, M., et al., 2014. Secondary organic aerosol yields of 12-carbon alkanes. Atmos. Chem. Phys. 14, 1423–1439.
Lu, Z., Hao, J., Takekawa, H., Hu, L., Li, J., 2009. Effect of high concentrations of inorganic seed aerosols on secondary organic aerosol formation in the m-xylene/NO_x photooxidation system. Atmos. Environ. 43, 897–904.
Mellouki, A., Le Bras, G., Sidebottom, H., 2003. Kinetics and mechanisms of the oxidation of oxygenated organic compounds in the gas phase. Chem. Rev. 103, 5077–5096.
Meyer, N.K., Duplissy, J., Gysel, M., Metzger, A., Dommen, J., Weingartner, E., et al., 2009. Analysis of the hygroscopic and volatile properties of ammonium sulphate seeded and unseeded SOA particles. Atmos. Chem. Phys. 9, 721–732.
Miyoshi, A., Hatakeyama, S., Washida, N., 1994. OH radical- initiated photooxidation of isoprene: An estimate of global CO production. J. Geophys. Res. Atmos. 99, 18779–18787.
Nah, T., McVay, R.C., Pierce, J.R., Seinfeld, J.H., Ng, N.L., 2017. Constraining uncertainties in particle-wall deposition correction during SOA formation in chamber experiments. Atmos. Chem. Phys. 17, 2297–2310.
Nelson, L., Rattigan, O., Neavyn, R., Sidebottom, H., Treacy, J., Nielsen, O.J., 1990. Absolute and relative rate constants for the reactions of hydroxyl radicals and chlorine atoms with a series of aliphatic alcohols and ethers at 298K. Int. J. Chem. Kinet. 22, 1111–1126.
Ng, N.L., Chhabra, P.S., Chan, A.W.H., Surratt, J.D., Kroll, J.H., Kwan, A.J., et al., 2007. Effect of NO_x level on secondary organic aerosol (SOA) formation from the photooxidation of terpenes. Atmos. Chem. Phys. 7, 5159–5174.
Nozière, B., Dziedzic, P., Córdova, A., 2009. Products and kinetics of the liquid-phase reaction of glyoxal catalyzed by ammonium ions (NH_4^+). J. Phys. Chem. A 113, 231–237.
Odum, J.R., Hoffmann, T., Bowman, F., Collins, D., Flagan, R.C., Seinfeld, J.H., 1996. Gas/particle partitioning and secondary organic aerosol yields. Environ. Sci. Technol. 30, 2580–2585.
Pöschl, U., 2005. Atmospheric aerosols: composition, transformation, climate and health effects. Angew. Chem. Int. Ed. 44, 7520–7540.
Powelson, M.H., Espelien, B.M., Hawkins, L.N., Galloway, M.M., De Haan, D.O., 2014. Brown carbon formation by aqueous-phase carbonyl compound reactions with amines and ammonium sulfate. Environ. Sci. Technol. 48, 985–993.
Presto, A.A., Huff Hartz, K.E., Donahue, N.M., 2005. Secondary organic aerosol production from terpene ozonolysis. 2. Effect of NO_x concentration. Environ. Sci. Technol. 39, 7046–7054.
Riva, M., Da Silva Barbosa, T., Lin, Y.H., Stone, E.A., Gold, A., Surratt, J.D., 2016. Chemical characterization of organosulfates in secondary organic aerosol derived from the photooxidation of alkanes. Atmos. Chem. Phys. 16, 11001–11018.
Robinson, C.B., Schill, G.P., Zarzana, K.J., Tolbert, M.A., 2013. Impact of organic coating on optical growth of ammonium sulfate particles. Environ. Sci. Technol. 47, 13339–13346.
Rudich, Y., Donahue, N.M., Mentel, T.F., 2007. Aging of organic aerosol: Bridging the gap between laboratory and field studies. Annu. Rev. Phys. Chem. 58, 321–352.
Sadezky, A., Chaimbault, P., Mellouki, A., Römpp, A., Winterhalter, R., Le Bras, G., et al., 2006. Formation of secondary organic aerosol and oligomers from the ozonolysis of enol ethers. Atmos. Chem. Phys. 6, 5009–5024.
Sakamoto, Y., Inomata, S., Hirokawa, J., 2013. Oligomerization reaction of the Criegee intermediate leads to secondary organic aerosol formation in ethylene ozonolysis. J. Phys. Chem. A 117, 12912–12921.
Sarrafzadeh, M., Wildt, J., Pullinen, I., Springer, M., Kleist, E., Tillmann, R., et al., 2016. Impact of NO_x and OH on secondary organic aerosol formation from β-pinene photooxidation. Atmos. Chem. Phys. 16, 11237–11248.
Schade, G.W., Dreyfus, G.B., Goldstein, A.H., 2002. Atmospheric methyl tertiary butyl ether (MTBE) at a rural mountain site in California. J. Environ. Qual. 31, 1088–1094.
Seinfeld, J.H., Pankow, J.F., 2003. Organic atmospheric particulate material. Annu. Rev. Phys. Chem. 54, 121–140.
Semadeni, M., Stocker, D.W., Kerr, J.A., 1993. Further studies of the temperature dependence of the rate coefficients for the reactions of OH with a series of ethers under simulated atmospheric conditions. J. Atmos. Chem. 16, 79–93.
Semelsberger, T.A., Borup, R.L., Greene, H.L., 2006. Dimethyl ether (DME) as an alternative fuel. J. Power Sources 156, 497–511.
Smith, D.F., Kleindienst, T.E., Hudgens, E.E., McIver, C.D., Bufalini, J.J., 1991. The photooxidation of methyl tertiary butyl ether. Int. J. Chem. Kinet. 23, 907–924.
Song, C., Na, K., Cocker, D.R., 2005. Impact of the hydrocarbon to NO_x ratio on secondary organic aerosol formation. Environ. Sci. Technol. 39, 3143–3149.
Song, C., Na, K., Warren, B., Malloy, Q., Cocker, D.R., 2007. Impact of propene on secondary organic aerosol formation from m-xylene. Environ. Sci. Technol. 41, 6990–6995.
Song, C., Wu, L., Xie, Y., He, J., Chen, X., Wang, T., et al., 2017. Air pollution in China: Status and spatiotemporal variations. Environ. Pollut. 227, 334–347.
Stirnweis, L., Marcolli, C., Dommen, J., Barmet, P., Frege, C., Platt, S.M., et al., 2017. Assessing the influence of NO_x concentrations and relative humidity on secondary organic aerosol yields from α-pinene photo-oxidation through smog chamber experiments and modelling calculations. Atmos. Chem. Phys. 17, 5035–5061.
Surratt, J.D., Murphy, S.M., Kroll, J.H., Ng, N.L., Hildebrandt, L., Sorooshian, A., et al., 2006. Chemical composition of secondary organic aerosol formed from the photooxidation of isoprene. J. Phys. Chem. A 110, 9665–9690.
Tang, Y., Ren, Q., Wen, Q., Yu, C., Xie, X., Hu, Q., et al., 2019. Effect of methyl tert-butyl ether on adipogenesis and glucose metabolism in vitro and in vivo. J. Environ. Sci. 85, 208–219.
Tsiligiannis, E., Hammes, J., Salvador, C.M., Mentel, T.F., Hallquist, M., 2019. Effect of NO_x on 1,3,5-trimethylbenzene (TMB) oxidation product distribution and particle formation. Atmos. Chem. Phys. 19, 15073–15086.
Volkamer, R., Ziemann, P.J., Molina, M.J., 2009. Secondary organic aerosol formation from acetylene (C_2H_2): seed effect on SOA yields due to organic photochemistry in the aerosol aqueous phase. Atmos. Chem. Phys. 9, 1907–1928.
Wang, S., Xing, J., Jang, C., Zhu, Y., Fu, J.S., Hao, J., 2011. Impact assessment of ammonia emissions on inorganic aerosols in East China using response surface modeling technique. Environ. Sci. Technol. 45, 9293–9300.
Wyche, K.P., Monks, P.S., Ellis, A.M., Cordell, R.L., Parker, A.E., Whyte, C., et al., 2009. Gas phase precursors to anthropogenic secondary organic aerosol: detailed observations of 1,3,5-trimethylbenzene photooxidation. Atmos. Chem. Phys. 9, 635–665.
Ye, S., Ma, T., Duan, F., Li, H., He, K., Xia, J., et al., 2019. Characteristics and formation mechanisms of winter haze in Changzhou, a highly polluted industrial city in the Yangtze River Delta, China. Environ. Pollut. 253, 377–383.
Yu, G., Bayer, A.R., Galloway, M.M., Korshavn, K.J., Fry, C.G., Keutsch, F.N., 2011. Glyoxal in aqueous ammonium sulfate solutions: Products, kinetics and hydration effects. Environ. Sci. Technol. 45, 6336–6342.
Zhang, R., Wang, G., Guo, S., Zamora, M.L., Ying, Q., Lin, Y., et al., 2015. Formation of urban fine particulate matter. Chem. Rev. 115, 3803–3855.
Zhang, X., Schwantes, R.H., Coggon, M.M., Loza, C.L., Schilling, K.A., Flagan, R.C., et al., 2014. Role of ozone in SOA formation from alkane photooxidation. Atmos. Chem. Phys. 14, 1733–1753.
Zhao, D., Schmitt, S.H., Wang, M., Acir, I.-H., Tillmann, R., Tan, Z., et al., 2018. Effects of NO_x and SO_2 on the secondary organic aerosol formation from photooxidation of α-pinene and limonene. Atmos. Chem. Phys. 18, 1611–1628.
Zhu, J., Tsona, N.T., Mellouki, A., Du, L., 2019. Atmospheric initiated oxidation of short chain aliphatic ethers. Chem. Phys. Lett. 720, 25–31.
Zhu, J., Wang, S., Tsona, N.T., Jiang, X., Wang, Y., Ge, M., et al., 2017. Gas-phase reaction of methyl n-propyl ether with OH, NO_3, and Cl: Kinetics and mechanism. J. Phys. Chem. A 121, 6800–6809.